Remote sensing of spatio-temporal relationships between the partitioned absorption coefficients of phytoplankton cells and mineral particles and euphotic zone depths in a partially mixed shelf sea

Catherine Mitchell, Alex Cunningham *

Physics Department, University of Strathclyde, 107 Rottenrow, Glasgow G40NG, UK

ABSTRACT

Absorption coefficients for mineral particles and phytoplankton cells in the 488 nm waveband, $a_{MSS}(488)$ and $a_{CHL}(488)$, and euphotic zone depths, $z_{1\%PAR}$, were determined for the Irish Sea and St. George's Channel from 8 years of MODIS remote sensing reflectance observations. The results are presented as composite maps of the entire region for the months of January, April, July and October and as time series averaged over 2 week intervals for three selected locations representing different mixing regimes. Annual cycles in $a_{MSS}(488)$ were observed in most areas, with maximum values occurring in winter when increased vertical mixing brought fine sediments to the surface. Euphotic depths were strongly influenced by $a_{MSS}(488)$ cycles, but sharp reductions were superimposed wherever phytoplankton blooms occurred. A key hydrographic feature of this region is the formation of a front in St. George's Channel between mixed and seasonally stratified water bodies. On the mixed side of the front, single peaks in $a_{CHL}(488)$ were observed in summer when the euphotic zone was at its deepest. On the stratified side, double peaks in $a_{CHL}(488)$ occurred in spring and autumn while low summer values of $a_{CHL}(488)$ coincided with high values of $z_{1\%PAR}$. The remote sensing evidence indicates, therefore, that phytoplankton growth (as reflected by net accumulation at the surface) in summer was limited by light availability in mixed waters, and nutrient availability in the stratified region. We conclude that observations of spatio-temporal patterns in phytoplankton and mineral particle absorption coefficients and euphotic depths derived from ocean colour sensors can provide insights into the processes determining the depth of penetration of solar radiation, and also the factors limiting near-surface primary production, in optically complex and spatially heterogeneous shelf seas.

1. Introduction

The patterns of primary production observed in shelf seas exhibit a challenging degree of dynamical complexity (Simpson & Sharples, 2012). It is important to understand the mechanisms which generate this complexity if we are to develop realistic numerical models of shelf sea ecosystems, and to gain insights into the likely response of these ecosystems to anthropogenic disturbance and climate change (Guenette, Araujo, & Bundy, 2014; Holt et al., 2014). Positive rates of net primary production, which require adequate light levels, are achieved in the euphotic zone which is often assumed to extend from the surface to the depth ($z_{1\%PAR}$) at which spectrally-integrated photosynthetically active radiation (PAR) falls to 1% of its surface value (Kirk, 2011). If phytoplankton growth is to be sustained, however, there is also a requirement for a supply of inorganic nutrients which are usually derived from the remineralisation of organic material in

benthic sediments (Schultz & Zabel, 2006). Consequently, physical mixing of the water column plays an important role in determining rates of primary production by transporting inorganic nutrients towards the surface from deeper water while simultaneously circulating phytoplankton cells through a light field which decreases exponentially with depth (Howarth, Simpson, Sundermann, & van Haren, 2002). Mathematical models which quantify this interdependence of light availability, nutrient supply and vertical mixing are capable in themselves of generating a rich variety of dynamic behaviour (Ryabov, Rudolf, & Blasius, 2010; Greenwood & Craig, 2014), but in a real water column there are additional complicating factors. These include (i.) the possible presence of non-phytoplankton modifiers of subsea light fields, such as coloured dissolved organic matter and suspended mineral particles (Vantrepotte et al., 2007) and (ii.) processes of advection and stratification which can introduce significant spatial and temporal decoupling between mixing events and phytoplankton growth (Peeters, Kerimoglu, & Straile, 2013). In a given region, therefore, observation of the timing and geographical distribution of phytoplankton blooms, and the degree to which they are correlated with euphotic zone depths, is an important key to understanding the

* Corresponding author. Tel.: +44 141 548 3474; fax: +44 141 552 2891.
E-mail address: a.cunningham@strath.ac.uk (A. Cunningham).

fundamental processes which sustain shelf sea ecosystems (van Ruth, Ganf, & Ward, 2010; Capuzzo et al., 2013; Jin et al., 2013). However the high degree of heterogeneity in many shelf sea areas makes it difficult to adequately capture this spatial and temporal variability using in-situ sampling techniques (Gohin, 2011).

Optical remote sensing from polar orbiting satellites appears to offer an attractive solution to this problem (Robinson, 2008; Blondeau-Patissier, Gower, Dekker, Phinn, & Brando, 2014). Obvious advantages include synoptic spatial mapping, daily overpasses for many shelf sea locations and, thanks to extensive existing infrastructure, relatively low resource requirements at the level of individual projects. There are also disadvantages, which include the possibility of significant primary production occurring below the remote sensing penetration depth (Gholamalifard, Esmaili-Sari, Abkar, Naimi, & Kutser, 2013; Frolov, Ryan, & Chavez, 2012) and biases arising from the fact that observations are always made around noon under cloud-free conditions (Eleveld, van der Wal, & van Kessel, 2014). A greater obstacle, however, arises from the uncertain performance of traditional, empirically-derived algorithms in shelf sea environments (Cui et al., 2010; Shang et al., 2014; Zhao et al., 2014). The approach to algorithm development adopted here is based on the Quasi-Analytical Algorithm (QAA) developed by Lee, Carder, and Arnone (2002), which aims to retrieve two inherent optical properties, the spectral absorption coefficients $a(\lambda)$ and backscattering coefficients $b_b(\lambda)$ from subsurface remote sensing reflectance $r_{rs}(\lambda)$. Once these inherent optical properties have been determined, they can be incorporated into secondary algorithms to generate values for irradiance attenuation coefficients (Lee et al., 2013), euphotic depths (Shang, Lee, & Wei, 2011; Soppa, Dinter, Taylor, & Bracher, 2013; Mitchell, Cunningham, & McKee, 2014a) and in specific cases concentrations of optically significant seawater constituents (Le & Hu, 2013; Mishra, Mishra, Lee, & Tucker, 2013). Moreover, in waters where the optical contribution of CDOM is constant (or so low that its variability can be neglected) particulate absorption coefficients recovered by the QAA can be resolved into separate components for phytoplankton cells and mineral particles (Mitchell, Cunningham, & McKee, 2014b).

The hypotheses which are tested in this paper are (i) that recently developed algorithms based on the QAA approach can significantly extend the capability of optical remote sensing in shelf seas, (ii) that these algorithms allow the mapping of spatial and temporal patterns of variability in euphotic depth and in the absorption coefficients for phytoplankton and mineral particles in the surface layer, and (iii) that relationships between these variables can be interpreted in terms of the interaction of physical factors (light penetration depth and the degree of water column mixing) in determining the magnitude and timing of phytoplankton blooms. The Irish Sea was selected as a test location because it provides a wide range of water types in a relatively restricted area, and its optical and hydrological properties have been the subject of a large number of previous studies: see for example Brown et al. (2003) for physical structure; Tilstone, Smyth, Gowen, Martinez-Vicente, and Groom (2005) and McKee and Cunningham (2006) for inherent optical properties and primary production; Gowen et al. (2008) for trophic status; Bowers, Roberts, White, and Moate (2013) for coloured dissolved organic matter; Smith, Stewart, and McDonald (2003) for suspended particles; and Holt, Proctor, Blackford, Allen, and Ashworth (2004) for physical/biological modelling. There are, however, striking gaps in the coverage of the region provided by ship based surveys. Studies of the south and west are fewer in number and tend to be concentrated at the junction with the Celtic Sea, and there is a marked absence of information regarding conditions in winter.

2. Methods

2.1. Geographical context

The work presented in this paper covers the Irish Sea and St. George's Channel (Fig. 1), whose bathymetric characteristics
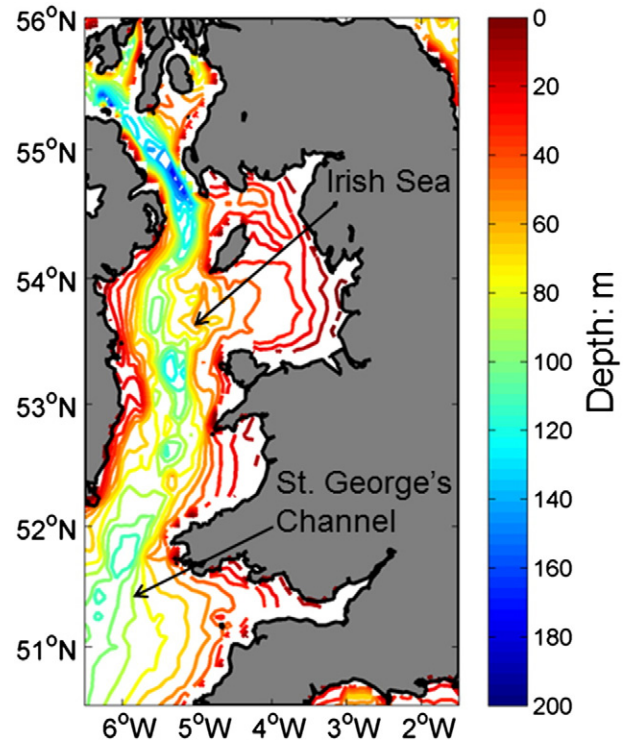

Fig. 1. Bathymetric contours for the Irish Sea and St. George's Channel.

include a deep (90 m–120 m) central trough bounded by broad shallow (20 m–50 m) shelves. In winter, the entire region is mixed by a combination of wind and tidal stirring (Bowers, 2003), but in summer stratified regions form in eastern bays, in deeper waters to the west of the Isle of Man, and in the south where St. George's Channel forms a link between the Irish and Celtic Seas (Simpson & Bowers, 1981). The approximate location of the front which forms between mixed and stratified waters in St. George's Channel is indicated by the change in sea surface temperature from 13 °C to 15 °C in Fig. 2.

This figure also shows the positions of three 11×11 pixel patches (each corresponding to an area at the sea surface of 8.5 km × 12 km) that were used to construct remote sensing time series, and two hydrographic stations from which optical profiles were obtained. Patch A (51.6°N, 6.16°W; depth 75 m) was located in the southern stratified zone, Patch B (52.8°N, 5.44°W; depth 60 m) in deep mixed water and Patch C (53.5°N, 4.71°W; depth 45 m) in shallower water with very strong tidal mixing (Ellis, Binding, Bowers, Jones, & Simpson, 2008). Station 50 (51.53°N, 6.33°W) was positioned near patch A and Station 43 (52.32°N, 5.94°W) mid-way between patches A and B.

2.2. Remote sensing data

MODIS (Moderate Resolution Imaging Spectroradiometer) Aqua data for the eight-year period from January 2005 to December 2013 were downloaded from the NASA Goddard Distributed Active Archive Center. Level-1A data were processed in SeaDAS 6.4, using the default 2-band aerosol model with an iterative near infra-red correction, to obtain remote sensing reflectance $R_{rs}(\lambda)$ at 1 km resolution in the visible wavebands. Pixels that were not masked by cloud or by proximity to the coastline were converted to subsurface reflectances, $r_{rs}(\lambda)$, using the relationship given in Lee et al. (2002):

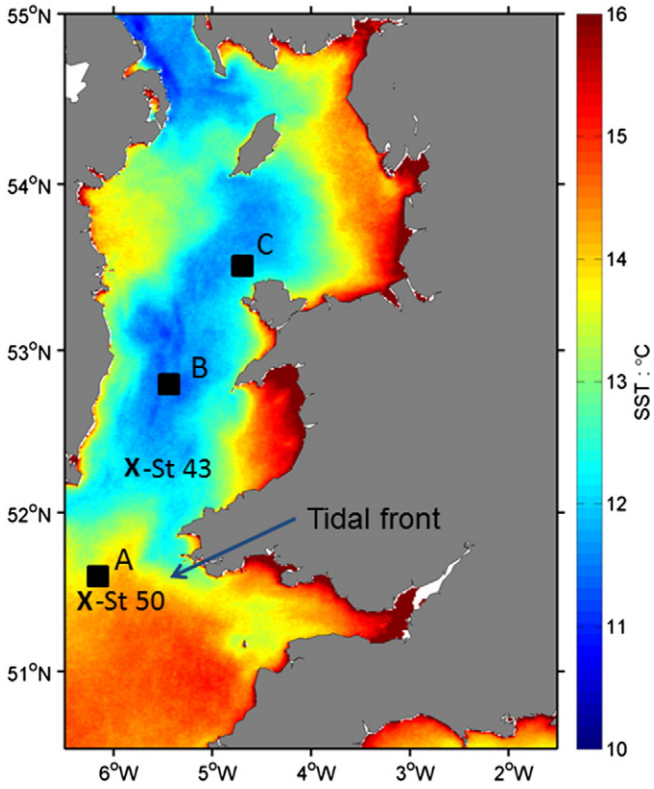$$r_{rs}(\lambda) = \frac{R_{rs}(\lambda)}{0.52 + 1.7R_{rs}(\lambda)} \qquad (1)$$

Fig. 2. MODIS sea surface temperature image of the Irish Sea and St. George's Channel for the month of June (a composite of all the data available from 2005 to 2013). The squares labelled A, B, and C indicate the 11 × 11 pixel patches used in the time series analysis (Figs. 6–8), and the crosses indicate the positions of two stations (St. 43 and St. 50) where the fluorescence and backscattering profiles shown in Fig. 15 were measured. The arrow shows the position of the seasonal front in St. George's Channel, which separates the mixed waters of the central Irish Sea to the north from the thermally stratified waters of the Celtic Sea to the south.

and mapped on a Mercator projection. Sea surface temperature (SST) data for all pixels with valid r_{rs} values in the visible wavebands were also generated from MODIS Aqua observations using SeaDAS. The

subsequent processing steps are described in detail below, and the overall sequence is summarised in Fig. 3.

2.3. Absorption coefficients

Total absorption and backscattering coefficients, $a(\lambda)$ and $b_b(\lambda)$, were derived from r_{rs} spectra using the procedure described in Mitchell et al. (2014b), which employs version 5 of the Quasi-Analytical Algorithm (Lee, Lubac, Werdell, & Arnone, 2009) with subsequent linearisation of the absorption coefficients. This procedure was tested using a modelled data set incorporating locally determined specific inherent optical properties. For the 488 nm waveband, the RMSE (root mean square error) values obtained were ± 0.003 m^{-1} for $b_b(488)$ and ± 0.004 m^{-1} for $a(488)$. The recovered absorption coefficients were partitioned to give the separate contributions of phytoplankton cells, $a_{CHL}(488)$, and mineral particles, $a_{MSS}(488)$, using the method proposed by Mitchell et al. (2014b). First, the absorption due to CDOM, $a_{CDOM}(488)$, was estimated by plotting particulate backscattering against non-water absorption (i.e. the known values for water absorption tabulated by Pope and Fry (1997) were subtracted from the total absorption coefficient recovered using the QAA). This step is only applicable to data sets where a consistent modal CDOM concentration can be assumed, but it has been shown to work well for all but coastal areas of the Irish Sea. Subtraction of the estimated value of $a_{CDOM}(488)$ and the known absorption coefficient for sea water, $a_w(488)$, gives values for the particulate component of the absorption coefficient, $a_p(488)$, which can be resolved into separate MSS and CHL components using

$$a_{MSS}(488) = \frac{b_{bp}(488) - \rho_2 a_p(488)}{\rho_1 - \rho_2} \qquad (2)$$

and

$$a_{CHL}(488) = \frac{\rho_1 a_p(488) - b_{bp}(488)}{\rho_1 - \rho_2} \qquad (3)$$
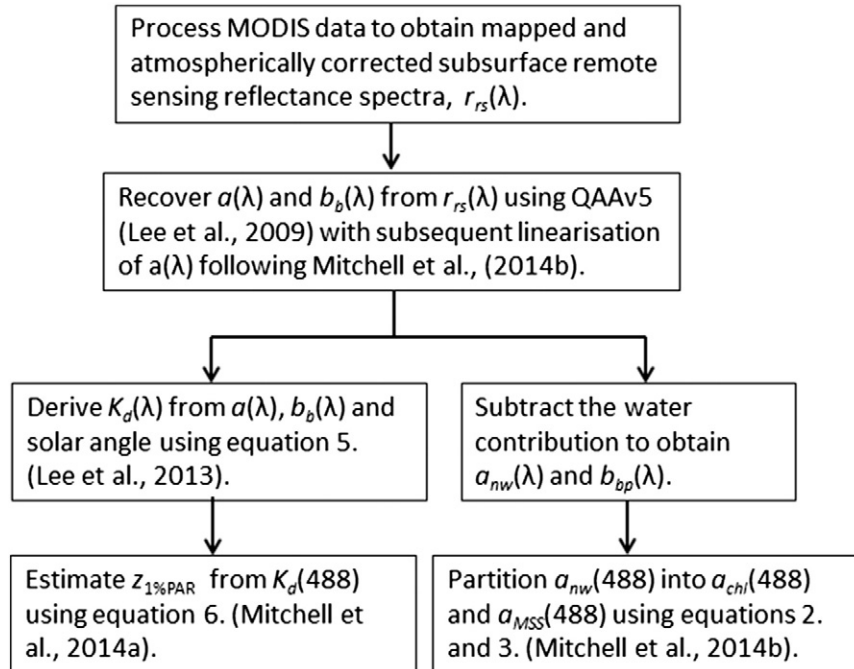

Fig. 3. Outline of the data processing sequence.

where

$$\rho_1 = \frac{b_{bMSS}(488)}{a_{MSS}(488)} \text{ and } \rho_2 = \frac{b_{bCHL}(488)}{a_{CHL}(488)}. \quad (4)$$

The values established by Mitchell et al. (2014b) for the Irish Sea and adjacent waters of $\rho_1(488) = 0.432$ and $\rho_2(488) = 0.057$ were used for the analysis presented in the present paper.

2.4. Attenuation coefficients

The attenuation coefficients for downward planar irradiance, $K_d(\lambda)$, are formally defined over an infinitesimal depth interval, but Lee, Du, and Arnone (2005) suggested that it was more practical to consider values averaged from the surface to the depth at which the irradiance reaches 10% of its surface value, and introduced the notation $\overline{K}_d(\lambda)$. A method for calculating these average values from $a(\lambda)$, $b_b(\lambda)$ and the solar angle (θ_s) was proposed by Lee et al. (2005) and validated for the Irish Sea by Cunningham, Ramage, and McKee (2013). However Lee et al. (2013) subsequently modified their model to account for the

spectral dependence of the scattering phase function, and derived the expression

$$\overline{K}_d(\lambda) = (1 + m_0\theta_s)(a(\lambda) + m_1(1 - \gamma\eta_w(\lambda))\left(1 - m_2 e^{-m_3 a(\lambda)}\right)b_b(\lambda) \quad (5)$$

where $m_0 = 0.005$, $m_1 = 4.259$, $m_2 = 0.52$, $m_3 = 10.8$ and $\gamma = 0.265$. For this paper, therefore, the performance of Eq. (5) was evaluated by comparing its performance using $a(\lambda)$ and $b_b(\lambda)$ values measured in situ at 145 stations in the Irish Sea (at the positions indicated in Figure 1 of Mitchell et al., 2014a) with $\overline{K}_d(\lambda)$ measured at the same time using a SeaWiFS Profiling Multichannel Radiometer (Satlantic) and the results are shown in Fig. 4. For the 490 nm waveband, which is used for calculating euphotic depths, the best fit line has a coefficient of determination (r^2) of 0.92 and a gradient of 1.1.

2.5. Euphotic depths

Three methods for obtaining euphotic depth ($z_{1\%PAR}$) from $\overline{K}_d(E_d, 490)$ were proposed independently by Lee et al. (2007), Cunningham et al. (2013) and Zhao et al. (2013). These methods were reviewed by Mitchell et al. (2014a) and found to produce roughly equivalent results
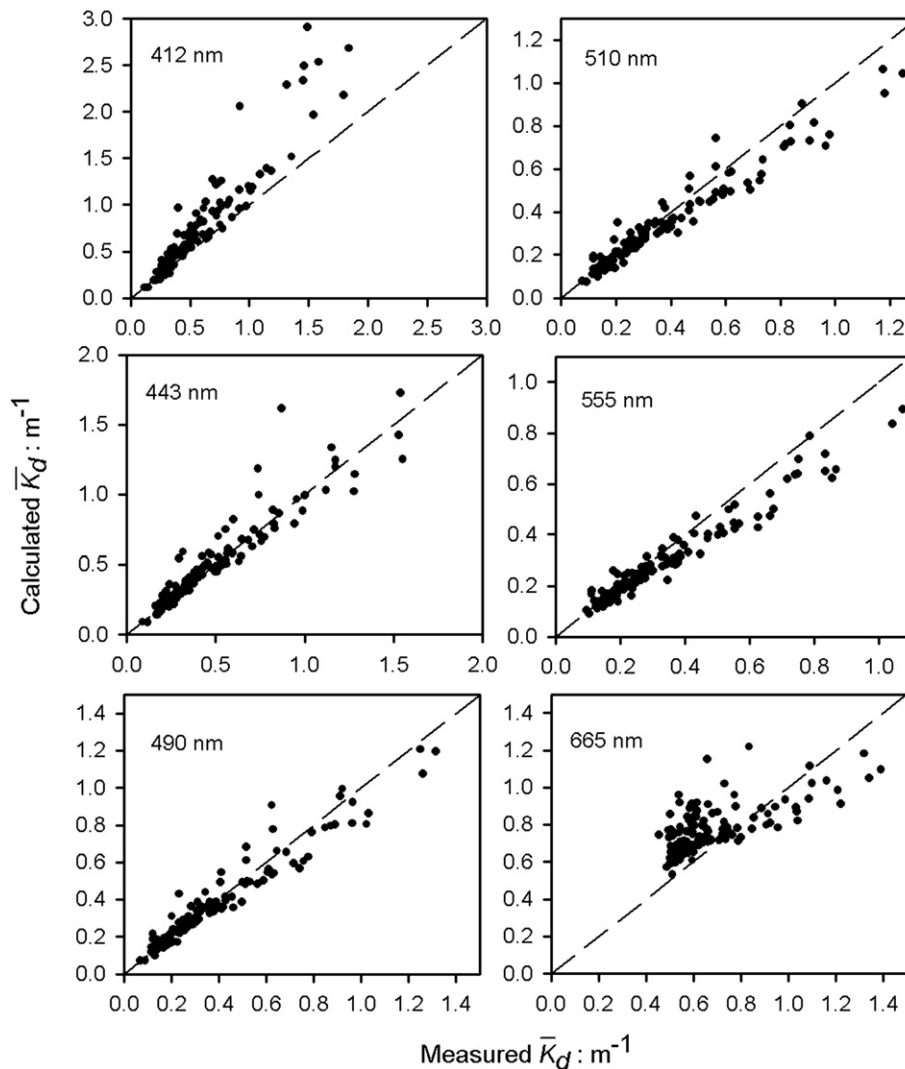

Fig. 4. Comparison of depth-averaged attenuation coefficients for downward irradiance, calculated using Eq. (5), with those measured in situ using a SeaWiFS Multichannel Profiling Radiometer.

when compared to in situ SPMR measurements for the Irish Sea, generating $z_{1\%PAR}$ values with average errors of around 20%. For the work presented here, the MODIS waveband centred on 488 nm was assumed to be functionally equivalent to the SeaWiFS band at 490 nm, and the relationship used was:

$$z_{1\%PAR} = 5.52\overline{K}_d(488)^{-0.86}. \qquad (6)$$

2.6. Optical time series

In order to investigate seasonal patterns in a_{MSS}, a_{CHL} and $z_{1\%PAR}$, time series were assembled for the three 11×11 pixel patches shown in Fig. 2. MODIS data were filtered so that only observations with a minimum of 60 non-clouded pixels in each patch were processed. The sequence of steps in Fig. 3 was then followed, and average values of the three variables for each patch were calculated.

2.7. Mean annual cycles

Mean annual cycles were derived by dividing the calendar year into two-week time intervals and calculating 8-year average values, denoted $\bar{a}_{MSS}(488)$, $\bar{a}_{CHL}(488)$, and $\bar{z}_{1\%PAR}$, for each interval. The standard deviations of the observations within each interval were used as an indicator of the extent of inter-annual variability in each time series.

2.8. Mapping

In an attempt to concisely capture spatial and temporal variability in $a_{MSS}(488)$, $a_{CHL}(488)$ and $z_{1\%PAR}$ for the Irish Sea region, contour maps were created for the months of January, April, July and October. At this latitude, these months are representative of winter, spring, summer and autumn, respectively. Composite data for each month were created by averaging all the observed values available for each pixel over the 8-year time series. The resolution of the composite images was reduced to 11×11 pixels in order to minimise spurious variability at high spatial frequencies, and contour maps generated for the three variables.

3. Results

3.1. Distribution of observations

The numbers of available observations in each two-week interval of the calendar year were plotted as histograms for positions A, B and C (Fig. 5).

For all three locations the frequency of observations was lowest in December and January, averaging around 15 per fortnight, and highest in June, averaging around 60 per fortnight. Thus only 13% of mid-day satellite passes were useable in winter and 54% in summer, indicating a requirement for a degree of interpolation or temporal averaging to compensate for the irregular nature of the remote sensing reflectance data.

3.2. Time series

When the data for $a_{MSS}(488)$, $a_{CHL}(488)$ and $z_{1\%PAR}$ were plotted as a function of time, marked annual periodicity in all three variables was observed (Figs. 6–8).

Mineral particle absorption, $a_{MSS}(488)$, was highest in January and lowest in the summer months at locations A, B and C, but there were differences in the amplitude and timing of the seasonal cycle. The highest $a_{MSS}(488)$ values, reaching a maximum 0.29 m^{-1}, were observed at position C, which was the shallowest of the three locations. At position B, in the deep central trough, the $a_{MSS}(488)$ maximum figure was 0.16 m^{-1}, and at position A, bordering on the open waters of the Celtic Sea, it was 0.05 m^{-1}. In spring, $a_{MSS}(488)$ values fell more quickly at A
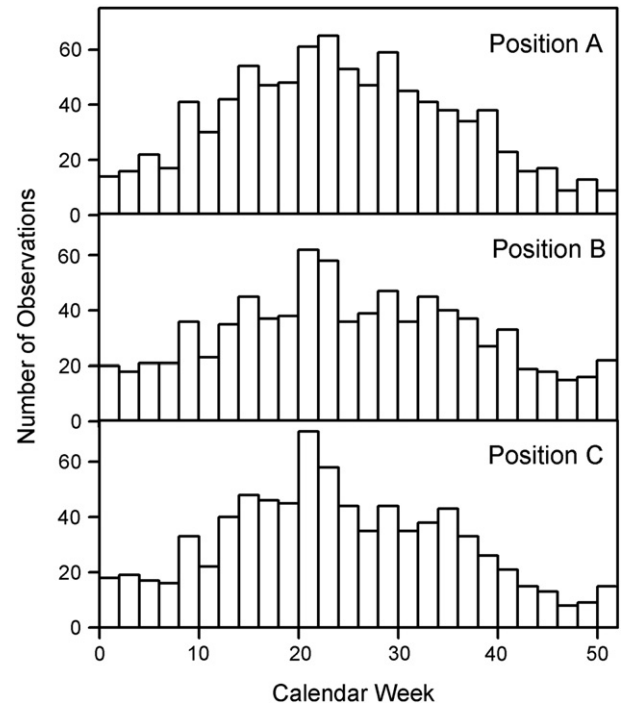

Fig. 5. Total number of MODIS observations in 2-week intervals for the 11×11 pixel patches located at positions A, B and C (see Fig. 2). Observations were used only if a minimum of 60 pixels in the patch were cloud-free.

than at B and C, but by mid-summer $a_{MSS}(488)$ at all three locations had fallen to below 0.05 m^{-1}.

The phytoplankton component of the absorption coefficient, $a_{CHL}(488)$, reached significantly higher peak values at position A (0.5 m^{-1}) than at B (0.13 m^{-1}) or C (0.25 m^{-1}). Interestingly, the year-to-year variability in $a_{CHL}(488)$ appeared to be higher than the variability in $a_{MSS}(488)$ at all three locations. This may indicate that the two variables respond differently to meteorological forcing, since the maintenance of mineral particles in the surface layer is largely dependent on wind mixing (Bowers, 2003), while phytoplankton growth is a function of both vertical mixing and light availability (Tilstone et al., 2005). Alternatively, short-lived peaks in phytoplankton absorption may not be fully resolved due to the irregular nature of the data coverage. In spite of this possible under-sampling, significant differences in the timing of the phytoplankton cycle between locations were apparent, with two peaks occurring in spring and autumn in most years at position A, and single midsummer peaks of much lower amplitude at B and C.

Euphotic depths, $z_{1\%PAR}$, became shallower in winter and deeper in summer at all three locations, but the range at A (5 m to 60 m) was significantly greater than at B (10 m to 45 m) and C (10 m to 40 m). There was a fairly clear inverse relationship between $a_{MSS}(488)$ and euphotic depth at B and C, but this relationship was less apparent at position A. The patterns of phytoplankton growth at locations A and B, and their relationships with euphotic depth, can be seen more clearly when data are plotted for a single year (Fig. 9).

3.3. Mean annual cycles

In order to emphasise the underlying seasonality in the data, averaged values ($\bar{a}_{MSS}(488)$, $\bar{a}_{CHL}(488)$, and $\bar{z}_{1\%PAR}$) were calculated for two week intervals over the whole time series. Clearly defined mean annual cycles were observed for mineral particle absorption at all three locations (Fig. 10).

There were interesting differences in timing, however, since $\bar{a}_{MSS}(488)$ declined from its winter maximum earlier in the year at A
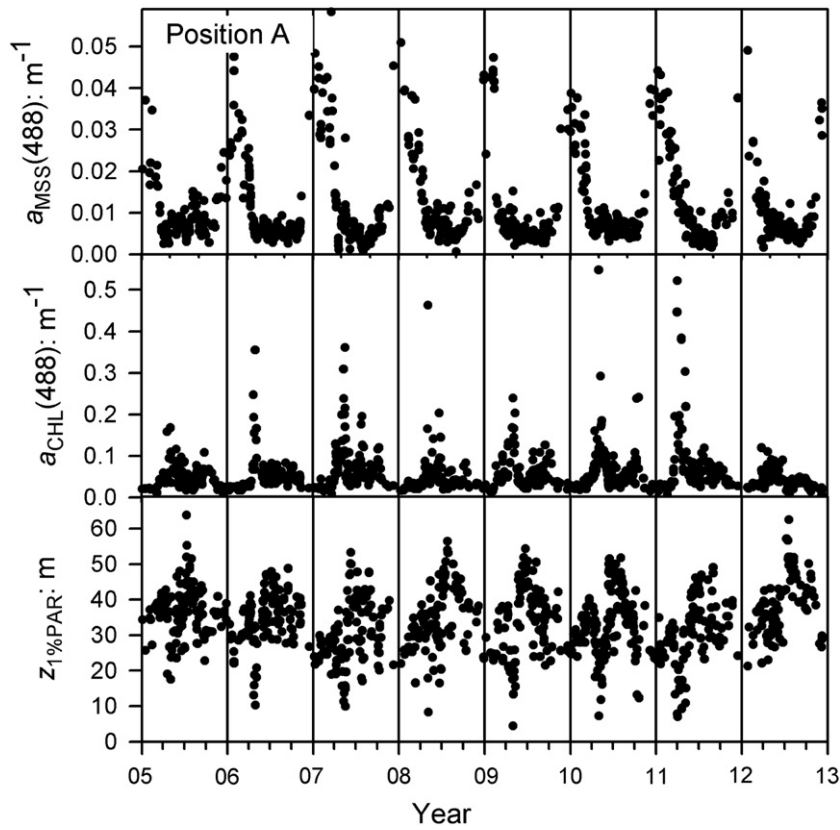
Fig. 6. 8-year time series showing all available observations for the absorption coefficients for suspended mineral particles, $a_{MSS}(488)$, and phytoplankton cells, $a_{CHL}(488)$, in the 488 nm waveband, together with euphotic depth, $z_{1\%PAR}$, at the 11 × 11 pixel patch located at position A, with central pixel coordinates 51.6°N, 6.16°W.
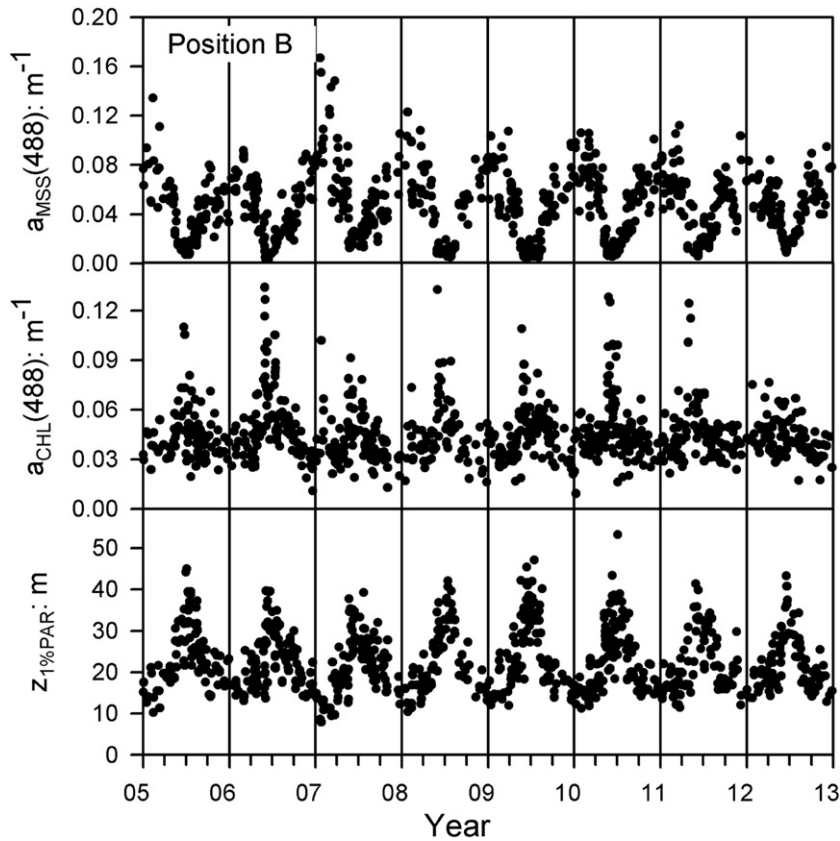
Fig. 7. 8-year time series showing all available observations for the absorption coefficients for suspended mineral particles, $a_{MSS}(488)$, and phytoplankton cells, $a_{CHL}(488)$, in the 488 nm waveband, together with euphotic depth, $z_{1\%PAR}$, at the 11 × 11 pixel patch located at position B, with central pixel coordinates 52.8°N, 5.44°W.
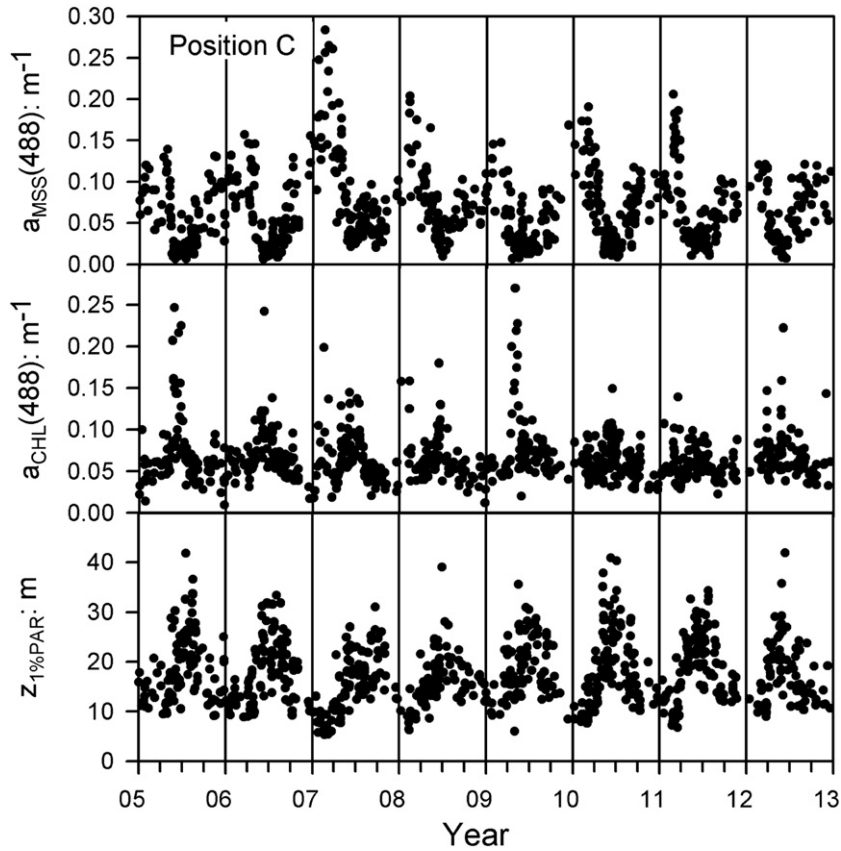
Fig. 8. 8-year time series showing all available observations for the absorption coefficients for suspended mineral particles, $a_{MSS}(488)$, and phytoplankton cells, $a_{CHL}(488)$, in the 488 nm waveband, together with euphotic depth, $z_{1\%PAR}$, at the 11×11 pixel patch located at position C, with central pixel coordinates 53.5°N, 4.7°W.
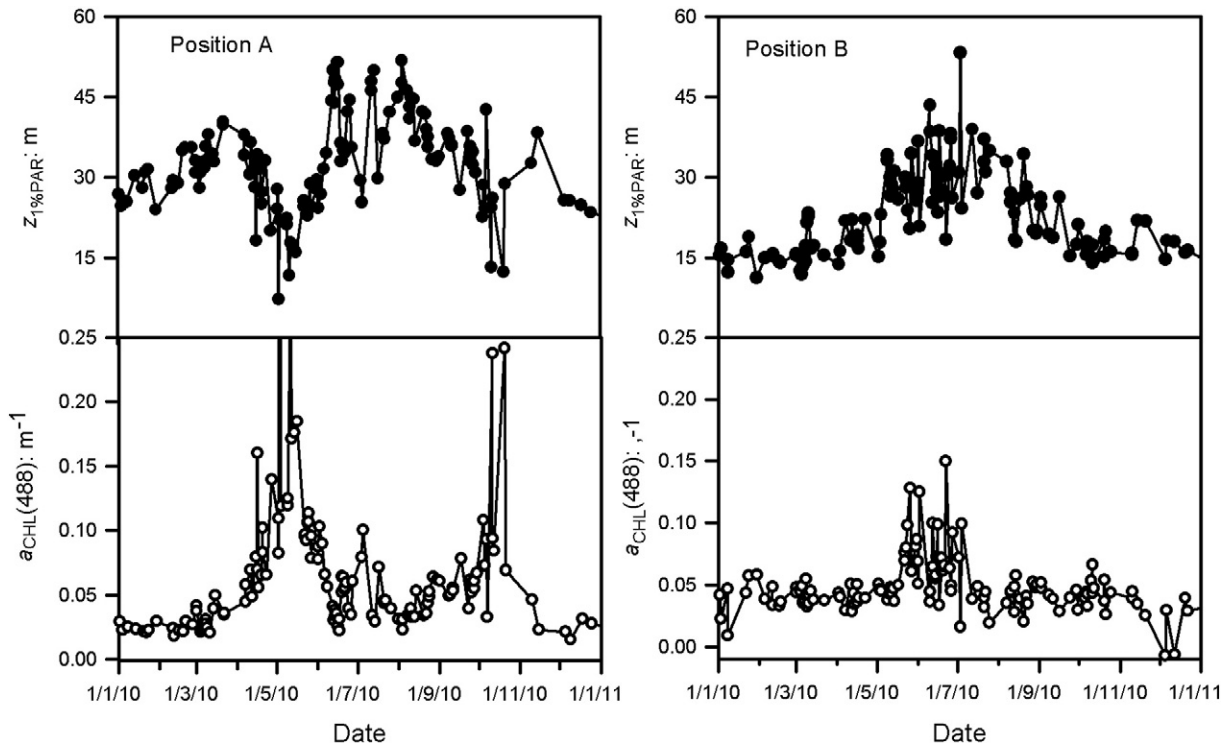

Fig. 9. Euphotic depths, $z_{1\%PAR}$, and phytoplankton absorption coefficients, $a_{CHL}(488)$, at positions A and B for the year 2010. At A, double peaks in $a_{CHL}(488)$ in spring and autumn coincide with minimum $z_{1\%PAR}$ values, whereas at B a single summer peak in $a_{CHL}(488)$ occurs when $z_{1\%PAR}$ values are at their highest.
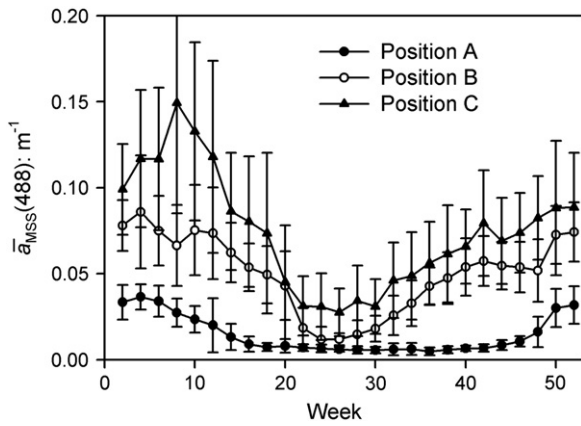
Fig. 10. Average annual cycles in the absorption coefficient for suspended mineral particles in the 488 nm MODIS waveband, $\bar{a}_{MSS}(488)$, calculated for the 8-year time series of observations at positions A, B and C. Symbols indicate mean values, and error bars standard deviations of the observations.

than at B and C, and recovered later. Consequently the 'summer' minimum in $\bar{a}_{MSS}(488)$ had an approximate duration of 30 weeks at A, but only 8 weeks at B and C. Mean phytoplankton absorption, $\bar{a}_{CHL}(488)$, exhibited marked spring and autumn peaks at A, while smaller mid-year elevations were observed at B and C (Fig. 11).

Mean euphotic depths, $\bar{z}_{1\%PAR}$, followed a pattern of winter lows and summer highs at all three locations, and were largely influenced by the $\bar{a}_{MSS}(488)$ cycles. There was little evidence of phytoplankton absorption
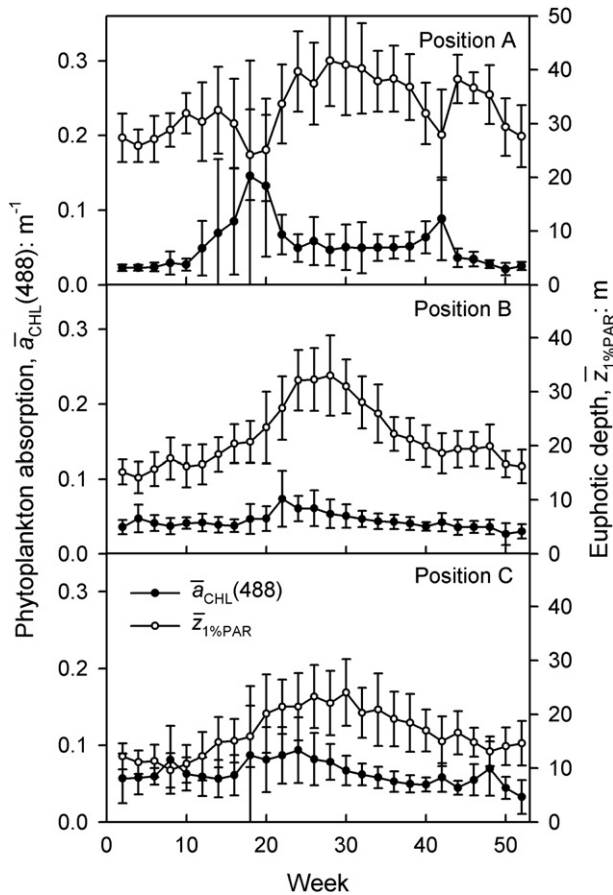

Fig. 11. Average annual cycles in euphotic depth, $\bar{z}_{1\%PAR}$, and the absorption coefficient for phytoplankton cells in the 488 nm MODIS waveband, $\bar{a}_{CHL}(488)$, calculated for the 8-year time series of observations at positions A, B and C. Symbols indicate mean values, and error bars standard deviations of the observations.

affecting euphotic depth at B and C (though these effects can be seen in the data before averaging), but clear reductions in $\bar{z}_{1\%PAR}$ accompanied the spring and autumn blooms at A. Comparison of the mean annual cycles in Fig. 11 with the time series in Figs. 6–8 suggests that two important features were obscured by the multi-year averaging process. One was the occurrence of well-defined mid-year peaks in chlorophyll absorption at position B. The second was the intensity of the reduction in euphotic depth at position A caused by the spring phytoplankton bloom, where $z_{1\%PAR}$ in some years fell below 10 m at a time when absorption by mineral particles was very low.

3.4. Monthly mapping

Maps of $\bar{a}_{MSS}(488)$, $\bar{a}_{CHL}(488)$, and $\bar{z}_{1\%PAR}$ calculated over the whole 8-year period for the months of January, April, July and October are shown in Figs. 12–14. For mineral particle absorption, the overall pattern in each month was strongly related to bathymetry, with the highest values occurring in shallower waters along coastlines and in estuaries (Fig. 12).

The annual cycles in $a_{MSS}(488)$ evident in the full time series are also clearly reflected in the monthly maps. More care is needed, however, in interpreting the maps of phytoplankton absorption (Fig. 13).

One problem is the sensitivity of the absorption partitioning algorithm to variable CDOM concentrations, which was modelled by Mitchell et al. (2014b). Values of $\bar{a}_{CHL}(488)$ in coastal locations where CDOM concentrations are likely to exceed 0.2 m^{-1} (according to Bowers et al., 2013) have therefore been marked as unreliable using asterisks, and the associated contours are indicated by broken lines. A second problem is the failure of monthly averaged maps to adequately represent the strength of the absorption peaks during periods of rapid phytoplankton growth, especially during the spring bloom in the south west. These issues indicate that it is necessary to take care in matching time scales when using remote sensing composites to assess the performance of numerical models of primary productivity.

The euphotic depth maps (Fig. 14) show a consistent spatial pattern of low values in estuaries and along the coasts and higher values in the deep central trough. Monthly-averaged euphotic depths are shallowest in winter and deepest in summer in all areas, ranging from below 10 m along the coasts in January to over 55 m in the south west in July. It should be noted, however, that these monthly averaged maps do not capture the marked reductions in $z_{1\%PAR}$ which occur, according to the time series, during periods of rapid phytoplankton growth.

4. Discussion

It is evident from the remote sensing time series (Figs. 6–8) that suspended mineral particles play a significant role in determining the optical properties of the Irish Sea and St. George's Channel, and that they are responsible for the winter reduction in the depth of penetration of solar radiation across the whole region. However phytoplankton can have a significant influence on euphotic depth at other times of the year. This is particularly obvious for the seasonally stratified position A, where the shallowest euphotic depths occur at the times of the spring blooms. Bowers (2003) and Neil, Cunningham, McKee, and Polton (2012) have shown that the presence of mineral particles in the surface layer of the Irish Sea depends on the input of mixing energy to the water column from winds and tides. This means that, in addition to providing information on an important determinant of the depth of the euphotic zone, the $a_{MSS}(488)$ signal can give insights into vertical mixing, whose significance in determining the phenology of phytoplankton growth is becoming increasingly recognised (Chiswell, 2011; Taylor & Ferrari, 2011). Since the depth of the water column greatly exceeds the euphotic depth in most of the Irish Sea and St. George's Channel, it is possible for mixing to transport phytoplankton cells out of the region
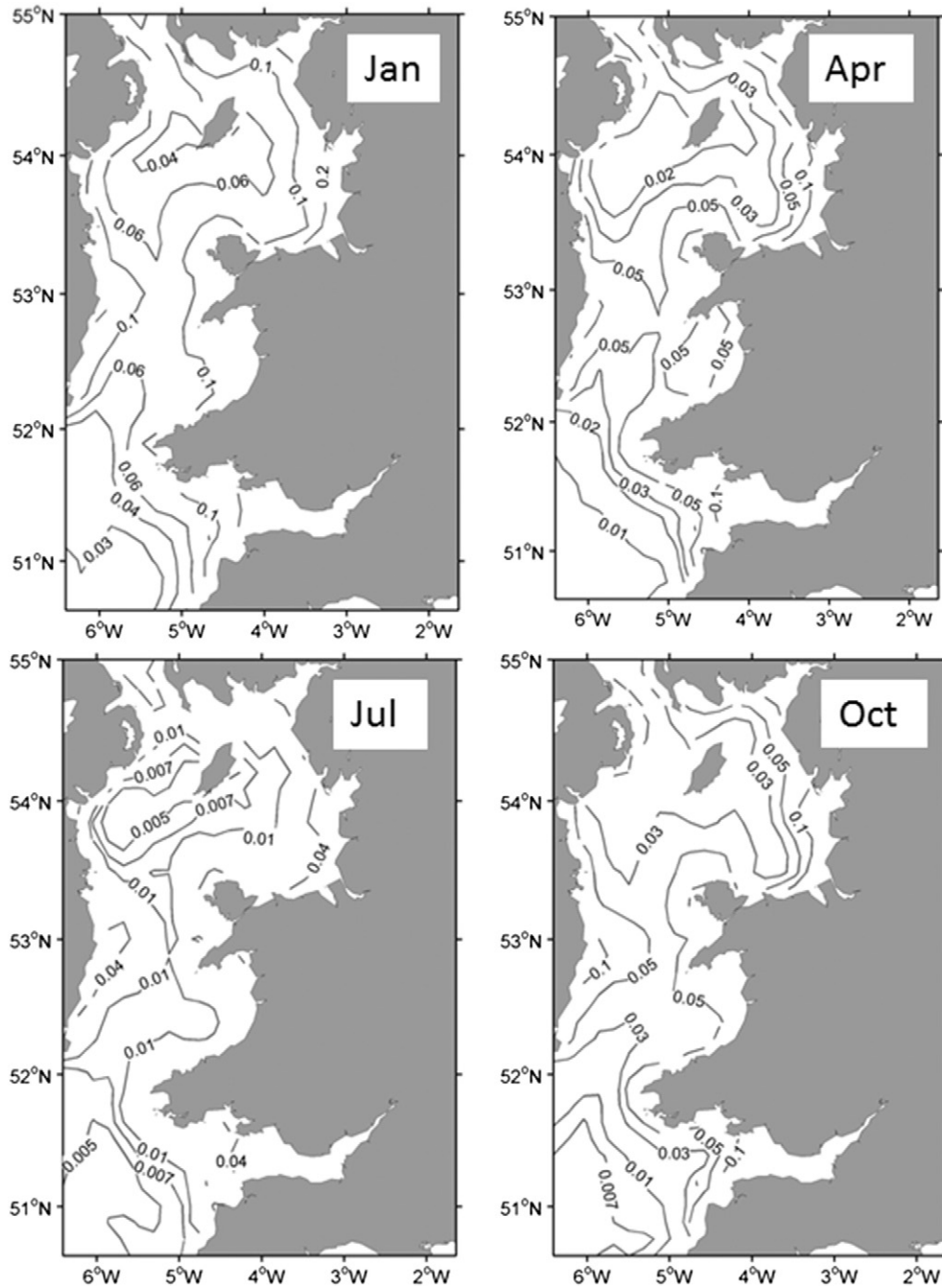
Fig. 12. Composite maps for mineral particle absorption coefficients, $a_{MSS}(488)$, calculated as averages for four calendar months over the 8-year time series.

where net primary production can be sustained. At position A, we observed (i.) low levels of $a_{MSS}(488)$ in the spring and summer months, indicating a prolonged reduction in vertical mixing and (ii.) a shallowing of the euphotic zone during the spring and autumn phytoplankton peaks, while low $a_{CHL}(488)$ values occurred in the middle of the year when the euphotic zone was deepest. These two observations suggest that phytoplankton growth (as reflected by net accumulation at the surface) at position A in summer was limited by a factor other than light, with the exhaustion of the mineral nutrient supply in the surface layer of a stratified water column being the most likely candidate. At B and C, on the other hand, mixing was more persistent and mineral particles were only able to settle out for a few weeks in the middle of the year. Phytoplankton absorption coefficients at these locations reached a maximum in mid-summer when euphotic depths were greatest,

implying that primary productivity at other times was limited by light availability. Since the euphotic depth exceeded 15 m for most of the year, this light limitation must have been due to deep water column mixing. Published studies using in situ data support this interpretation of the remote sensing evidence. The dependence of the timing of annual cycles in Irish Sea phytoplankton growth on subsea light levels is discussed by Gowen and Stewart (2005). The exhaustion of mineral nutrients in spring in the stratified waters in the south of our region of interest is documented by Pemberton, Rees, Miller, Raine, and Joint (2004), and the persistence of non-limiting concentrations of nitrate in the mixed waters of the central Irish Sea was noted by Gowen, Stewart, Mills, and Elliott (1995).

On the other hand, the physical limitations of remote sensing as a means of assessing primary production must also be acknowledged.
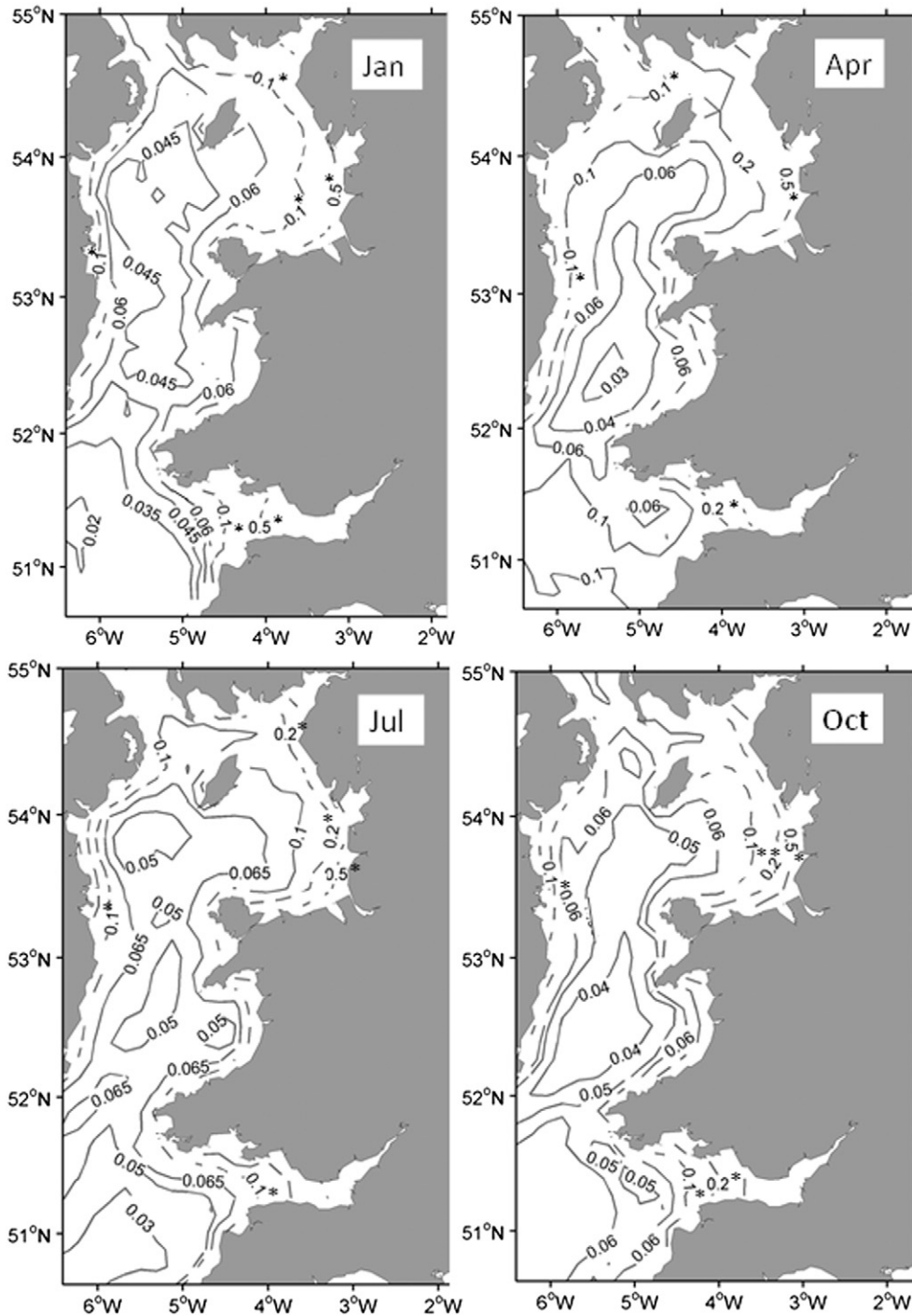
Fig. 13. Composite maps for phytoplankton absorption coefficients, a_{CHL}(488), calculated as averages for four calendar months over the 8-year time series. Values identified by asterisks and the contours indicated with dotted lines indicate coastal areas where the absorption partitioning algorithm is unreliable due to interference by coloured dissolved organic matter.

Fig. 15 shows profiles measured using a Hydroscat 2 (Hobilabs) during a cruise in July 2002 at two stations located on either side of the front in St. George's Channel. CTD data (not shown) confirmed that Station 43 was fully mixed, while Station 50 was stratified. The variables plotted are backscattering at 470 nm, which largely originates from suspended mineral particles, and fluorescence at 676 nm, which can be treated as a proxy for phytoplankton concentration. Typical euphotic depths and remote sensing depths (calculated as the inverse of the attenuation coefficient at 488 nm) for these locations are indicated as broken lines on the plots. At the mixed station there was a uniform distribution of

fluorescence and backscattering with depth. The stratified station, on the other hand, had a low backscattering signal at the surface which increased with depth, showing the loss of mineral particles from the surface layer to deeper waters. There was also a strong fluorescence peak at around 20 m, indicating a deep chlorophyll maximum which was presumably dependent on nutrients crossing the pycnocline (Sharples et al., 2001). Since the chlorophyll layer was located below the remote sensing penetration depth, it is likely that annual primary production values derived from ocean colour observations would be under-estimates in these stratified waters.
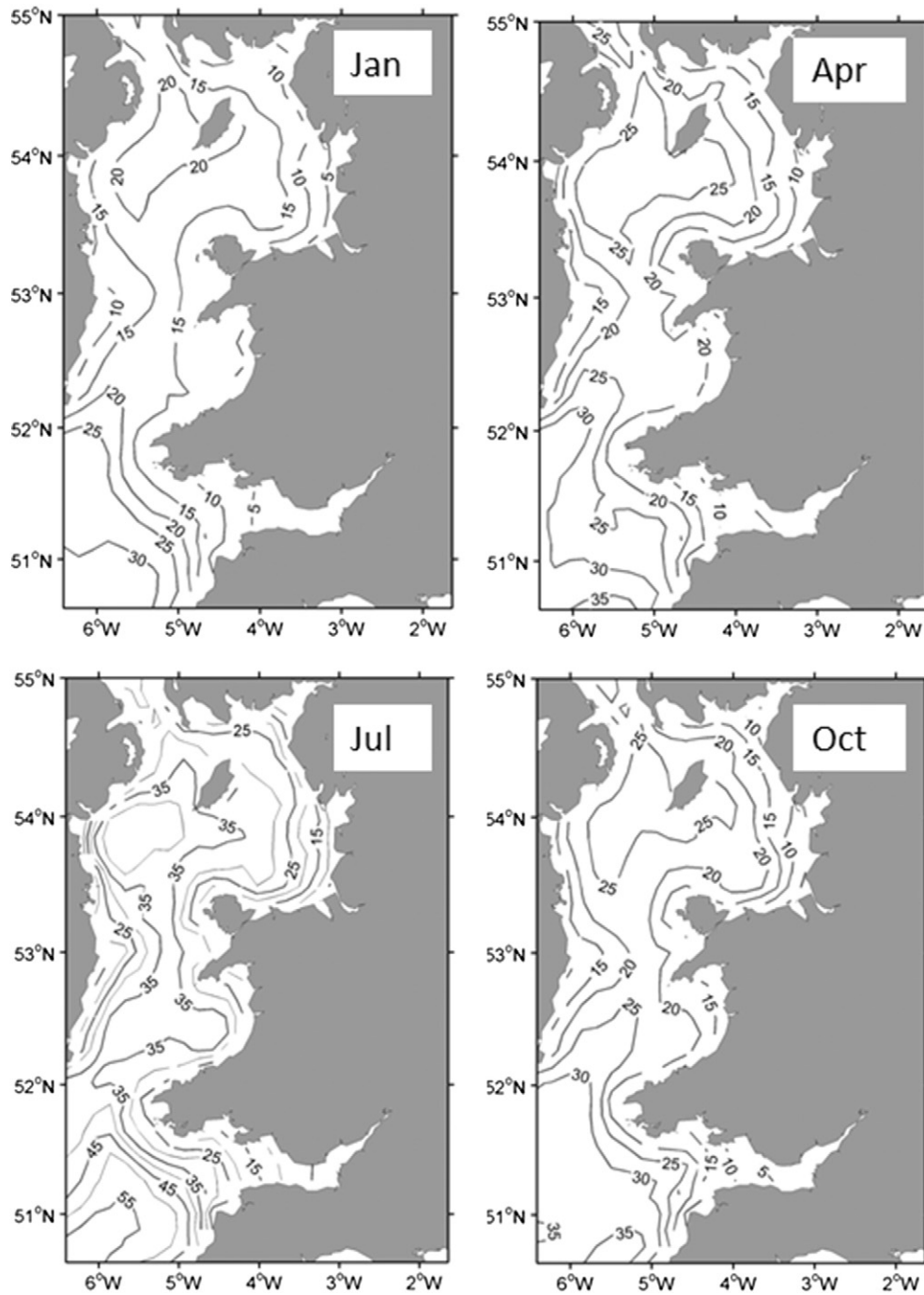
Fig. 14. Composite maps for euphotic depths, $z_{1\%PAR}$, calculated as averages for four calendar months over the 8-year time series.

5. Conclusion

The initial aim of this work was to investigate whether recent progress on the remote sensing of euphotic depths (Mitchell et al., 2014a) and the partitioning of particulate absorption coefficients (Mitchell et al., 2014b) could be combined to give insights into phytoplankton dynamics in a shelf sea environment. This proved to be challenging for the Irish Sea, since the high incidence of cloud cover produced gaps in the observing sequence which led to difficulties in fully resolving the dynamics of short-duration phytoplankton blooms. The employment of multi-year averaging made it possible to establish characteristic seasonal cycles for the region, but also had the effect of smoothing out the apparent amplitude of the blooms and their influence on euphotic depths. Nevertheless, monthly composite maps

produced by this technique provided information on spatial and temporal patterns in the absorption coefficients for phytoplankton cells and mineral particles, together with euphotic depths, with a coverage greatly exceeding that obtainable from ship-based surveys. These maps provide useful baselines for measuring changes in the Irish Sea system in response to eutrophication and climate change. Their use for constraining numerical models of shelf sea ecosystems, however, depends on model outputs being averaged to match the temporal resolution of the remote sensing observations. The contrast in phytoplankton phenology between stratified and mixed waters, and its implications for light versus nutrient limitation, was an unexpected outcome of this work. We conclude that time series of $a_{MMS}(488)$, $a_{CHL}(488)$ and $z_{1\%PAR}$ values derived by remote sensing can provide useful insights into the interaction of light penetration, mixing rates, and nutrient
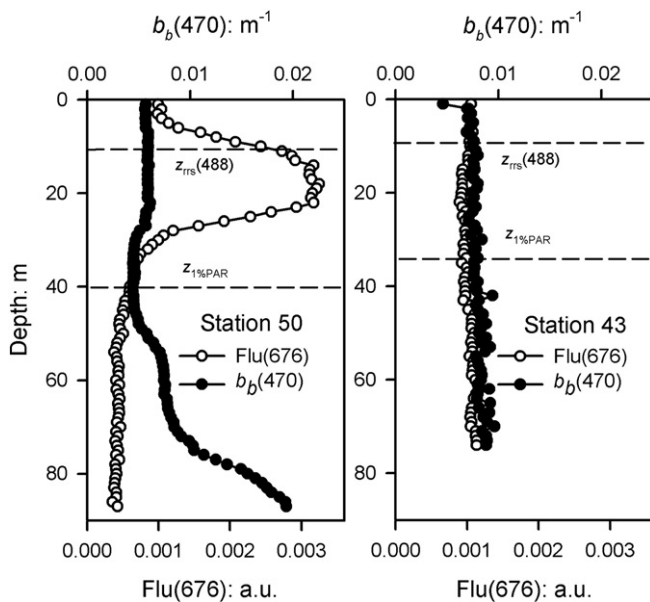
Fig. 15. Profiles of the backscattering coefficient at 470 nm, $b_b(470)$, and phytoplankton fluorescence at 676 nm, $Flu(676)$ measured using a Hydroscat 2 at Station 50 (51.53°N, 6.33°W) and Station 43 (52.3°N, 5.94°W) in July 2002. These data were acquired and processed using the procedures described in Mitchell et al. (2014a). The broken lines indicate remote sensing penetration depths at 488 nm, $z_{rrs}(488)$, and euphotic depths, $z_{1\%PAR}$, for July at these locations.

availability in a partially mixed shelf sea. This lends support to the emerging idea that applications of ocean colour remote sensing, even in optically challenging conditions, can extend beyond estimates of seawater composition to studies of physical forcing factors and their impact on ecosystem dynamics (Taylor & Ferrari, 2011; Navarro et al., 2012). These encouraging results suggest that it would be worthwhile to devote resources to validate the remote sensing products derived in this paper using match-ups between satellite observations and in situ measurements. Such validation would best be attempted, however, in a shelf sea region which was less subject to cloud cover than the Irish Sea.

Acknowledgements

References

Blondeau-Patissier, D., Gower, J.F.R., Dekker, A.G., Phinn, S.R., & Brando, V.E. (2014). A review of ocean color remote sensing methods and statistical techniques for the detection, mapping and analysis of phytoplankton blooms in coastal and open oceans. *Progress in Oceanography, 123*, 123–144.

Bowers, D.G. (2003). A simple turbulent energy-based model of fine suspended sediments in the Irish Sea. *Continental Shelf Research, 23*, 1495–1505.

Bowers, D.G., Roberts, E.M., White, M., & Moate, B.D. (2013). Water masses, mixing, and the flow of dissolved organic carbon through the Irish Sea. *Continental Shelf Research, 58*, 12–20.

Brown, J., Carrillo, L., Fernand, L., Horsburgh, K.J., Hill, A.E., Young, E.F., et al. (2003). Observations of the physical structure and seasonal jet-like circulation of the Celtic Sea and St. George's Channel of the Irish Sea. *Continental Shelf Research, 23*, 533–561.

Capuzzo, E., Painting, S.J., Forster, R.M., Greenwood, N., Stephens, D.T., & Mikkelsen, O.A. (2013). Variability in the sub-surface light climate at ecohydrodynamically distinct sites in the North Sea. *Biogeochemistry, 113*, 85–103.

Chiswell, S.M. (2011). Annual cycles and spring blooms in phytoplankton: Don't abandon Sverdrup completely. *Marine Ecology Progress Series, 443*, 39–50.

Cui, T.W., Zhang, J., Groom, S., Sun, L., Smyth, T., & Sathyendranath, S. (2010). Validation of MERIS ocean-color products in the Bohai Sea: A case study for turbid coastal waters. *Remote Sensing of Environment, 114*, 2326–2336.

Cunningham, A., Ramage, L., & McKee, D. (2013). Relationships between inherent optical properties and the depth of penetration of solar radiation in optically complex coastal waters. *Journal of Geophysical Research, Oceans, 118*, 2310–2317.

Eleveld, M.A., van der Wal, D., & van Kessel, T. (2014). Estuarine suspended particulate matter concentrations from sun-synchronous satellite remote sensing: Tidal and meteorological effects and biases. *Remote Sensing of Environment, 143*, 204–215.

Ellis, K.M., Binding, C.E., Bowers, D.G., Jones, S.E., & Simpson, J.H. (2008). A model of turbidity maximum maintenance in the Irish Sea. *Estuarine Coastal and Shelf Science, 76*, 765–774.

Frolov, S., Ryan, J.P., & Chavez, F.P. (2012). Predicting euphotic-depth-integrated chlorophyll-a from discrete-depth and satellite-observable chlorophyll-a off Central California. *Journal of Geophysical Research, Oceans, 117*, C05042.

Gholamalifard, M., Esmaili-Sari, A., Abkar, A., Naimi, B., & Kutser, T. (2013). Influence of vertical distribution of phytoplankton on remote sensing signal of Case II waters: Southern Caspian Sea case study. *Journal of Applied Remote Sensing, 7*, 073550.

Gohin, F. (2011). Annual cycles of chlorophyll-a, non-algal suspended particulate matter, and turbidity observed from space and in-situ in coastal waters. *Ocean Science, 7*, 705–732.

Gowen, R.J., & Stewart, B.M. (2005). The Irish Sea: Nutrient status and phytoplankton. *Journal of Sea Research, 54*, 36–50.

Gowen, R.J., Stewart, B.M., Mills, D.K., & Elliott, P. (1995). Regional differences in stratification and its effect on phytoplankton production and biomass in the north western Irish Sea. *Journal of Plankton Research, 17*, 753–769.

Gowen, R.J., Tett, P., Kennington, K., Mills, D.K., Shammon, T.M., Stewart, B.M., et al. (2008). The Irish Sea: Is it eutrophic? *Estuarine, Coastal and Shelf Science, 76*, 239–254.

Greenwood, J., & Craig, P. (2014). A simple numerical model for predicting vertical distribution of phytoplankton on the continental shelf. *Ecological Modelling, 273*, 165–172.

Guenette, S., Araujo, J.N., & Bundy, A. (2014). Exploring the potential effects of climate change on the Western Scotian Shelf ecosystem, Canada. *Journal of Marine Systems, 134*, 89–100.

Holt, J., Allen, J.B., Anderson, T.R., Brewin, R., Butenshon, M., Harle, J., et al. (2014). Challenges in integrative approaches to modelling the marine ecosystems of the North Atlantic: Physics to fish and coasts to ocean. *Progress in Oceanography, 129*, 285–313.

Holt, J.T., Proctor, R., Blackford, J.C., Allen, J.I., & Ashworth, M. (2004). Advective controls on primary production in the stratified western Irish Sea: An eddy-resolving model study. *Journal of Geophysical Research, Oceans, 109*, C05024.

Howarth, M.J., Simpson, J.H., Sundermann, J., & van Haren, H. (2002). Processes of Vertical Exchange in Shelf Seas (PROVESS). *Journal of Sea Research, 47*, 199–208.

Jin, J., Liu, S.M., Ren, J.L., Liu, C.G., Zhang, J., Zhang, G.L., et al. (2013). Nutrient dynamics and coupling with phytoplankton species composition during the spring blooms in the Yellow Sea. *Deep Sea Research Part II: Topical Studies in Oceanography, 97*, 16–32.

Kirk, J.T.O. (2011). *Light and photosynthesis in aquatic ecosystems.* Cambridge University Press.

Le, C.F., & Hu, C.M. (2013). A hybrid approach to estimate chromophoric dissolved organic matter in turbid estuaries from satellite measurements: A case study for Tampa Bay. *Optics Express, 21*, 18849–18871.

Lee, Z.P., Carder, K.L., & Arnone, R. (2002). Deriving inherent optical properties from water color: A multi-band quasi-analytical algorithm for optically deep waters. *Applied Optics, 41*, 5755–5772.

Lee, Z.P., Du, K.P., & Arnone, R. (2005). A model for the diffuse attenuation coefficient of downwelling irradiance. *Journal of Geophysical Research, Oceans, 110*, C02016.

Lee, Z., Hu, C., Shang, S., Du, K., Lewis, M., Arnone, R., et al. (2013). Penetration of UV–visible solar radiation in the global oceans: Insights from ocean color remote sensing. *Journal of Geophysical Research, Oceans, 118*, C02308.

Lee, Z.P., Lubac, B., Werdell, J., & Arnone, W. (2009). *An update of the Quasi-Analytical Algorithm (QAAv5).* Dartmouth, Canada: International Ocean Colour Coordinating Group.

Lee, Z., Weidemann, A., Kindle, J., Arnone, R., Carder, K.L., & Davis, C. (2007). Euphotic zone depth: Its derivation and implication to ocean-color remote sensing. *Journal of Geophysical Research, Oceans, 112*, C03009.

McKee, D., & Cunningham, A. (2006). Identification and characterisation of two optical water types in the Irish Sea from in situ inherent optical properties and seawater constituents. *Estuarine, Coastal and Shelf Science, 68*, 305–316.

Mishra, S., Mishra, D.R., Lee, Z., & Tucker, C.S. (2013). Quantifying cyanobacterial phycocyanin concentration in turbid productive waters: A quasi-analytical approach. *Remote Sensing of Environment, 133*, 141–151.

Mitchell, C., Cunningham, A., & McKee, D. (2014a). Remote sensing of shelf sea optical properties: Evaluation of a quasi-analytical approach for the Irish Sea. *Remote Sensing of Environment, 143*, 142–153.

Mitchell, C., Cunningham, A., & McKee, D. (2014b). Remote sensing of particulate absorption coefficients and their biogeochemical interpretation: A case study in the Irish Sea. *Remote Sensing of Environment, 152*, 74–82.

Navarro, G., Caballero, I., Prieto, L., Vazquez, A., Flecha, S., Huertas, I.E., et al. (2012). Seasonal-to-interannual variability of chlorophyll-a bloom timing associated with physical forcing in the Gulf of Cadiz. *Advances in Space Research, 50*, 1164–1172.

Neil, C., Cunningham, A., McKee, D., & Polton, J.A. (2012). Remote sensing of seasonal stratification dynamics in the southern Irish Sea. *Remote Sensing of Environment, 127*, 288–297.

Peeters, F., Kerimoglu, O., & Straile, D. (2013). Implications of seasonal mixing for phytoplankton production and bloom development. *Theoretical Ecology, 6*, 115–129.

Pemberton, K., Rees, A.P., Miller, P.I., Raine, R., & Joint, I. (2004). The influence of water body characteristics on phytoplankton diversity and production in the Celtic Sea. *Continental Shelf Research, 24*, 2011–2028.

Pope, R.M., & Fry, E.S. (1997). Absorption spectrum (380–700 nm) of pure water. II. Integrating cavity measurements. *Applied Optics, 36*, 8710–8723.

Robinson, I.S. (Ed.). (2008). *Remote sensing of shelf sea ecosystems. Marine Board Position Paper, 12,* . European Science Foundation.

Ryabov, A.B., Rudolf, L., & Blasius, B. (2010). Vertical distribution and composition of phytoplankton under the influence of an upper mixed layer. *Journal of Theoretical Biology, 263*, 120–133.

Schultz, H.D., & Zabel, M. (Eds.). (2006). *Marine geochemistry*. Berlin: Springer-Verlag.

Shang, S.L., Dong, Q., Hu, C.M., Lin, G., Li, Y.H., & Shang, S.P. (2014). On the consistency of MODIS chlorophyll a products in the northern South China Sea. *Biogeosciences, 11*, 269–280.

Shang, S., Lee, Z., & Wei, G. (2011). Characterization of MODIS-derived euphotic zone depth: Results for the China Sea. *Remote Sensing of Environment, 115*, 180–186.

Sharples, J., Moore, C.M., Rippeth, T.P., Holligan, P.M., Hydes, D.J., Fisher, N.R., et al. (2001). Phytoplankton distribution and survival in the thermocline. *Limnology and Oceanography, 46*, 486–496.

Simpson, J.H., & Bowers, D. (1981). Models of stratification and frontal movement in shelf seas. *Deep Sea Research, 28*, 727–738.

Simpson, J.H., & Sharples, J. (2012). *Introduction to the physical and biological oceanography of shelf seas.* Cambridge University Press.

Smith, C.N., Stewart, T.H., & McDonald, P. (2003). Results from an intensive measurement programme for suspended particulate matter in a region of the Irish Sea between Anglesey and the Isle of Man. *Continental Shelf Research, 23*, 1005–1018.

Soppa, M.A., Dinter, T., Taylor, B.B., & Bracher, A. (2013). Satellite derived euphotic depth in the Southern Ocean: Implications for primary production modelling. *Remote Sensing of Environment, 137*, 198–211.

Taylor, J.R., & Ferrari, R. (2011). Shutdown of turbulent convection as a new criterion for the onset of spring phytoplankton blooms. *Limnology and Oceanography, 56*, 2293–2307.

Tilstone, G.H., Smyth, T.J., Gowen, R.J., Martinez-Vicente, V., & Groom, S.B. (2005). Inherent optical properties of the Irish Sea and their effect on satellite primary production algorithms. *Journal of Plankton Research, 27*, 1127–1148.

van Ruth, P.D., Ganf, G.G., & Ward, T.M. (2010). Hot-spots of primary productivity: An alternative interpretation to conventional upwelling models. *Estuarine, Coastal and Shelf Science, 90*, 142–158.

Vantrepotte, V., Brunet, C., Meriaux, X., Lecuyer, E., Vellucci, V., & Santer, R. (2007). Bio-optical properties of coastal waters in the Eastern English Channel. *Estuarine, Coastal and Shelf Science, 72*, 201–212.

Zhao, J., Barnes, B., Melo, N., English, D., Lapointe, B., Muller-Karger, F., et al. (2013). Assessment of satellite-derived diffuse attenuation coefficients and euphotic depths in South Florida coastal waters. *Remote Sensing of Environment, 131*, 38–50.

Zhao, W.J., Wang, G.Q., Cao, W.X., Cui, T.W., Wang, G.F., Ling, J.F., et al. (2014). Assessment of SeaWiFS, MODIS, and MERIS ocean colour products in the South China Sea. *International Journal of Remote Sensing, 35*, 4252–4274.